Article

Effect of *abc* Pressing at 573 K on the Microstructure and Martensite Transformation Temperatures in Ti$_{49.8}$Ni$_{50.2}$ (at%)

Oleg Kashin *, Aleksandr Ivanovich Lotkov [ID], Victor Grishkov, Konstantin Krukovskii, Dorzhima Zhapova, Yuri Mironov, Natalia Girsova, Olga Kashina and Elena Barmina

Institute of Strength Physics and Materials Science of the Siberian Branch of the Russian Academy of Sciences, 634055 Tomsk, Russia; lotkov@ispms.ru (A.I.L.); grish@ispms.tsc.ru (V.G.); kvk@ispms.tsc.ru (K.K.); dorzh@ispms.tsc.ru (D.Z.); myp@ispms.ru (Y.M.); girsova@ispms.tsc.ru (N.G.); ocash@ispms.tsc.ru (O.K.); barmina@ispms.tsc.ru (E.B.)
* Correspondence: okashin@ispms.ru; Tel.: +7-382-228-69-20

Abstract: This paper presents experimental data on the microstructure and martensite transformation temperatures of Ti$_{49.8}$Ni$_{50.2}$ (at%) after *abc* pressing (multi-axial forging) to different true strains *e* from 1.84 to 9.55 at 573 K. The data show that increasing the true strain results in grain–subgrain refinement on different scales at a time. With *e* = 9.55 at 573 K, the average grain–subgrain size measured approximately 130 nm. Decreasing the *abc* pressing temperature from 723 to 573 K caused a decrease in all martensite transformation temperatures, a change in the lattice parameters, R phase formation, and angular shifts of diffraction peaks and their broadening. The largest change in the microstructure of Ti$_{49.8}$Ni$_{50.2}$ was provided by *abc* pressing to *e* = 1.84. Increasing the true strain to *e* = 9.55 resulted in a much smaller effect, suggesting that the alloy obtained a high density of structural defects even at *e* = 1.84. Two possible mechanisms of grain–subgrain refinement are discussed.

Keywords: TiNi; isothermal *abc* pressing; microstructure; grain–subgrain refinement; martensite transformation temperatures

1. Introduction

The mechanical and functional properties of polycrystalline metals and alloys are determined in many respects by the degree of their grain–subgrain refinement [1,2] and, hence, the average size of grains–subgrains can be considered one of the key microstructural factors responsible for almost all characteristics of metals and alloys. Among the promising methods of grain refinement is severe plastic deformation (SPD). By now, abundant experimental data are available showing that such refinement increases the hardness of materials [1–8]. The main outcome desired from SPD is an optimum average grain size that can provide a material with a high strength and acceptable plasticity. Another no less important outcome is a minimum possible grain and average grain–subgrain size, which is of interest for fundamental research in grain refinement mechanisms and for practical use in SPD materials. Obviously, achieving such outcomes needs knowledge of grain refinement mechanisms in metals and alloys exposed to severe plastic deformation. As has been shown [8], the refinement of grains under severe plastic deformation is controlled by two main sets of parameters: (1) SPD parameters, including the strain, its rate, temperature, and path; (2) material parameters, including the initial average grain size and staking fault energy.

Certainly, because of numerous factors of influence, it is challenging to propose a unified grain refinement mechanism for all metals and alloys and for all SPD methods. In available reviews [1–8], one can find brief descriptions of grain refinement models and mechanisms in metals and alloys exposed to different SPD methods and references to respective original works.

Some of these models describe the division of a grain in terms of partial-disclination nucleation and motion and associated misorientation of adjacent grain fragments due to the plastic strain accommodation in the grain. It is assumed that on approaching a certain critical grain size, diffusion accommodation of disclinations starts to dominate and no further grain refinement is possible. According to estimates [9], the relative temperature of transition from one mechanism of partial-disclination elastic energy accommodation to another during equal channel angular pressing (ECAP) is $\approx 0.65 T_m$ for fcc metals and $0.33 T_m$ for bcc ones (T_m is the melting temperature). Increasing the SPD temperature increases the minimum possible grain size.

The most widespread grain refinement models are those for metals and alloys that acquire a cellular dislocation substructure early in their deformation [1,8]. This type of model suggests that dislocations and other crystalline defects (vacancies, interstitial atoms) appear, move, and interact in SPD materials. Increasing the dislocation density in a grain results in a cellular dislocation substructure with low-angle cell boundaries and increasing the dislocation density in cell walls causes misorientation accumulation between adjacent cells with gradual transformation of low-angle boundaries or at least its large part into high-angle grain boundaries. As the strain is further increased, this process occurs in newly formed fine grain (finer than initial), ensuring additional grain refinement. It is assumed that the average dislocation cell size, d, is inversely proportional to the square root of the total dislocation density, ρ [1]:

$$d \sim \rho^{-1/2}, \tag{1}$$

From this assumption, the average size of grains during their refinement cannot reach values smaller than 100 nm [1]. Besides, at a certain critical grain size d_c, diffusion accommodation of dislocations in cell walls dominates [8], and their density increases slightly. The critical grain size, d_c, decreases with an increasing strain rate and increases with increasing temperature.

Actually, the minimum grain size attainable in an SPD process is determined by a certain dynamic balance between the generation of dislocations into the volume of a grain and their recovery from the volume via their escape to grain–subgrain boundaries or annihilation of dislocations with Burgers vectors of opposite sign. One of the mechanisms of dynamic dislocation recovery from cell walls can be non-conservative transverse dislocation glide with vacancy diffusion.

In materials highly prone to twinning at high strain rates and/or low strain temperatures, the mechanism of grain refinement includes the formation of packets of nanotwins that transform into nanograins via twin or matrix lamella fragmentation due to the twin boundary interaction with dislocations or shear bands [8]. In such refinement, the minimum grain size is much smaller than that ensured by gradual transformation of dislocation cell structures into an ultrafine grain structure due to the dislocation glide and diffusion motion of point defects.

The above examples of SPD-induced grain refinement are not exhaustive and other models are surely available. Nevertheless, these examples allow quite definite conclusions about the influence of individual factors on the mechanisms of grain structure transformation under SPD. In particular, there is no doubt that decreasing the SPD temperature leads to more efficient grain refinement. However, at relatively low temperatures, the load on equipment increases steeply and failure of test specimens becomes a risk. Therefore, in most related studies, the strain temperature is somewhat lower or higher than $T = 0.4 T_m$, where T_m is the melting temperature of a metal or alloy, i.e., the deformation is warm.

Note that the developed models are based mainly on experimental studies of copper, aluminum, nickel, titanium, iron, and their alloys, and the applicability of the models to TiNi is left almost untouched [10–39]. In our opinion, this is due to the insufficient systematic experimental data on TiNi alloys, and, in particular, on their structure and properties at different SPD temperatures. Bridging this gap needs experiments on TiNi alloys of specified compositions for analyzing the formation of their microstructure and

physico-mechanical properties under the same SPD conditions but at different strain temperatures.

By now, a number of studies of TiNi alloys, including near-equiatomic binary ones, are available to grasp the idea of their grain refinement at different SPD temperatures. For example, research data on TiNi alloys exposed to high strains by ECAP at 673–823 K [10–13] show that the alloys at temperatures above 773 K experience an intense dynamic recrystallization characteristic for increased temperatures, which does not allow for the formation of their ultrafine-grained (UFG) structure, and that the optimum ECAP temperature for their efficient grain refinement with no risk of failure of technological equipment is 723 K. Increasing the number of ECAP passes to eight provides the formation of an UFG structure with an average grain size of $\leq$0.25 μm, but the formation of a substantial nanocrystalline fraction with a grain size of $\leq$100 nm at this temperature fails [13]. It is supposed that for the formation of a nanocrystalline structure in bulk TiNi alloys, the ECAP temperature should be decreased to below 623 K [12]. Another paper reports that even in stainless-steel shells, Ti–50Ni and Ti–50.1Ni (at%) fail when deformed by ECAP at room temperature [14]. Unfortunately, no data on grain sizes are reported in the cited paper.

Research data are also available on the grain–subgrain structure of $Ti_{49.8}Ni_{50.2}$ specimens exposed to *abc* pressing (multi-axial forging) with their true strain set from 2.2 to 1.5 or equal to $\approx$3.6 at each step of the strain temperature successively decreased from 873 K to 573 K [15–18]. Actually, such pressing conditions mean that each temperature step of *abc* pressing is applied to specimens with a different initial grain–subgrain structure. The research data show that after *abc* pressing at 673 K, the alloy is dominated by a submicrocrystalline structure with a grain–subgrain size of 300–700 nm, and after *abc* pressing at 573 K (total true strain *e* = 7.7), the submicrocrystalline structure is refined to a grain–subgrain size of 100–500 nm, and at strain band intersections, to 2–100 nm with an estimated nanocrystalline fraction of no more than 30%.

After *abc* pressing to *e* = 8.44 at 723 K [19–22], this type of alloy acquires an inhomogeneous grain–subgrain structure with an average grain size of approximately 1 μm that comprises fine-grained, submicrocrystalline, and nanocrystalline fractions. It is noted that intense recovery processes develop in the alloy *abc* pressed at 723 K.

Thus, the previous studies show that equal channel angular pressing and *abc* pressing at a temperature of 773–673 K provide binary TiNi-based alloys mostly with a submicrocrystalline structure having an average grain–subgrain size of <1 μm.

Reasoning from these studies, it might be expected that isothermal severe plastic deformation at temperatures lower than the temperature range of warm deformation can provide more substantial grain refinement in TiNi-based alloys and a larger effect on their physico-mechanical properties, including inelastic ones. Here, we analyzed the grain–subgrain structure, phase state, and martensite transformation temperatures in $Ti_{49.8}Ni_{20.2}$ (at%) *abc* pressed to different true strains at 573 K.

2. Materials and Methods

The test material was $Ti_{49.8}Ni_{50.2}$ (at%) supplied by MATEK-SMA Ltd. (Moscow, Russia). Its specimens were made as described in detail elsewhere [22]. The initial specimens, which were shaped as a cube with a side of 20 mm via a single *abc* pressing cycle at 1073 K, were placed in dies, aged at 573 K for 10 min, and compressed on a hydraulic press with a rate of 0.16–0.18 s^{-1}. The decrease in the specimen temperature at the end of each compression event was no greater than 10 K. Each *abc* pressing cycle included compressive hits in three mutually perpendicular directions. After each compression event, the specimens were removed from their dies and again placed in them without cooling to deform the specimens in a direction perpendicular to the previous one. The cycle of three compression events was repeated several times to bring the specimens to their specified strain. After single pressing in one direction, the true strain was from *e* $\approx$ 0.15 to *e* $\approx$ 0.30. Thus, the specimens were deformed to a true strain of 1.84, 3.60, 5.40, 7.43, and 9.55.

The temperatures of martensite transformations were determined at an experimental set (ISPMS SB RAS, Tomsk, Russia) by a four-point method of measuring the temperature dependence of the electrical resistivity. The samples were made in the form of rods with a square cross-section of 1×1 mm^2 and a length of 20 mm. Two current and two potential electrodes were fixed to the sample by spot welding. The sample temperature was measured with a chromel–alumel thermocouple. The sample temperature was changed at a cooling/heating rate of 3 K/min. The temperatures of martensitic transformations were determined by tangents to the graphs of the temperature dependence of the electrical resistivity. The accuracy of estimating the martensitic transformations temperatures using this method was ± 2 K.
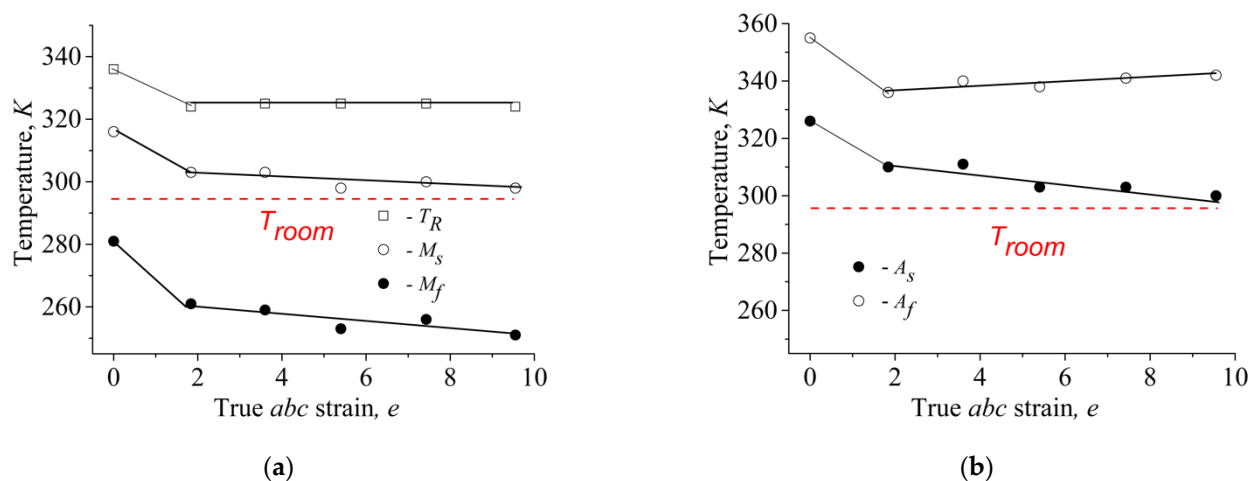
The microstructure of the alloy was analyzed on an Axiovert-200M inverted light microscope (Carl Zeiss AG, Oberkochen, Germany), a LEO EVO 50 XVP scanning electron microscope (Carl Zeiss AG, Oberkochen, Germany), and a JEM-2100 transmission electron microscope (JEOL Ltd., Tokyo, Japan). All equipment was provided by the NANOTECH Shared Use Center of ISPMS SB RAS (Tomsk, Russia). For the analysis, specimen slices were cut on electro-erosion machine. The slices were mechanically polished on a Saphir 350 grinding and polishing machine (Audit Diagnostics, Business & Technology Park, Carrigtwohill, Co., Cork, Ireland) using a SiC abrasive with a gradual decrease in its grit to 1200, finished with a diamond paste grained to 3 µm and etched in a mixture of nitric acid, hydrofluoric acid, and water with a ratio of 1:4:5.

For transmission electron microscopy (TEM), thin foils were prepared for which thin plates of a thickness of 0.5 mm were cut from the *abc* pressed specimens by electro-erosion cutting and were then either polished in an electrolyte containing sulfuric, nitric, and hydrofluoric acids in a ratio 6:1:3 or etched on an EM-09 100 15 ion slicer (JEOL Ltd., Tokyo, Japan). The crystalline structure of the alloy and its phase state were also analyzed by X-ray diffraction (XRD) on a DRON-7 diffractometer with the PDWin software (JSC Burevestnik, Russia) in Co-Kα radiation at room temperatures. The phase compositions of the samples were analyzed using crystallographic data on the structures of the phases B19$'$ (space group P2$_1$/m [40]) and R (space group P3 [41]). In the analysis, the ratio of the intensity of the doublet lines K$_{\alpha 2}$ and K$_{\alpha 1}$ was assumed at 0.52. The asymmetry of the intensity of the reflex profile was assumed at 1.1. The separation of the doublet (112)$_R$ and (300)$_R$ R phases was determined by the minimum value of the standard deviations of the sum of the profiles of these components from the experimental profile. The parameters of the crystal lattices of the phases were calculated using the positions of the maxima of the reflex profiles after separation. The B19$'$ lattice parameters were estimated from 10 reflections in the deformed alloy and from 14 reflections in the initial one. The R lattice parameters were estimated from reflections (11-2) and (300). Errors in the lattice parameters are shown in corresponding dependences on true strain.

3. Results

3.1. Temperatures of Martensite Transformation

Figure 1 shows the temperatures of martensite transformations in Ti$_{49.8}$Ni$_{50.2}$ versus the true *abc* strain. Here, M$_S$ and M$_f$ are the start and finish temperatures of direct B2→R→B19$'$ transformation on cooling, A$_S$ and A$_f$ are the start and finish temperatures of reverse martensite transformation on heating, T$_R$ is the start temperature of B2→R transformation, and T$_{room}$ is the room temperature (dashed line).
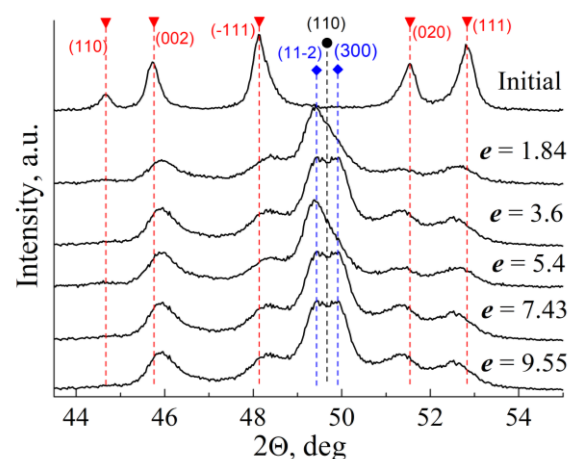
Figure 1. Martensite transformation temperatures versus true *abc* strain in Ti$_{49.8}$Ni$_{50.2}$: (**a**) on cooling; (**b**) on heating.

As can be seen from Figure 1a, the sequence of direct transformations in all specimens was B2→R→B19′. It can also be seen that the martensite transformation temperatures decreased steeply, even after *abc* pressing to *e* = 1.84. As the true strain further increased, the temperature T$_R$ remained almost unchanged, and the temperatures M$_S$ and M$_f$ decreased linearly with *e*. The temperature interval between M$_S$ and M$_f$ remained nearly constant for all values of *e*.

From Figure 1b, it can be seen that the temperatures A$_S$ and A$_f$ first decreased steeply, and as the strain increased, the temperature A$_S$ decreased slightly from 310 K in the specimens with *e* = 1.84 to 300 K in those with *e* = 9.55, whereas the temperature A$_f$ increased somewhat. Thus, increasing the true strain *e* increased the temperature interval between A$_S$ and A$_f$.

3.2. Phase States

Figure 2 shows fragments of the XRD spectra recorded in Ti$_{49.8}$Ni$_{50.2}$ at room temperature before and after *abc* pressing to different true strains *e*.
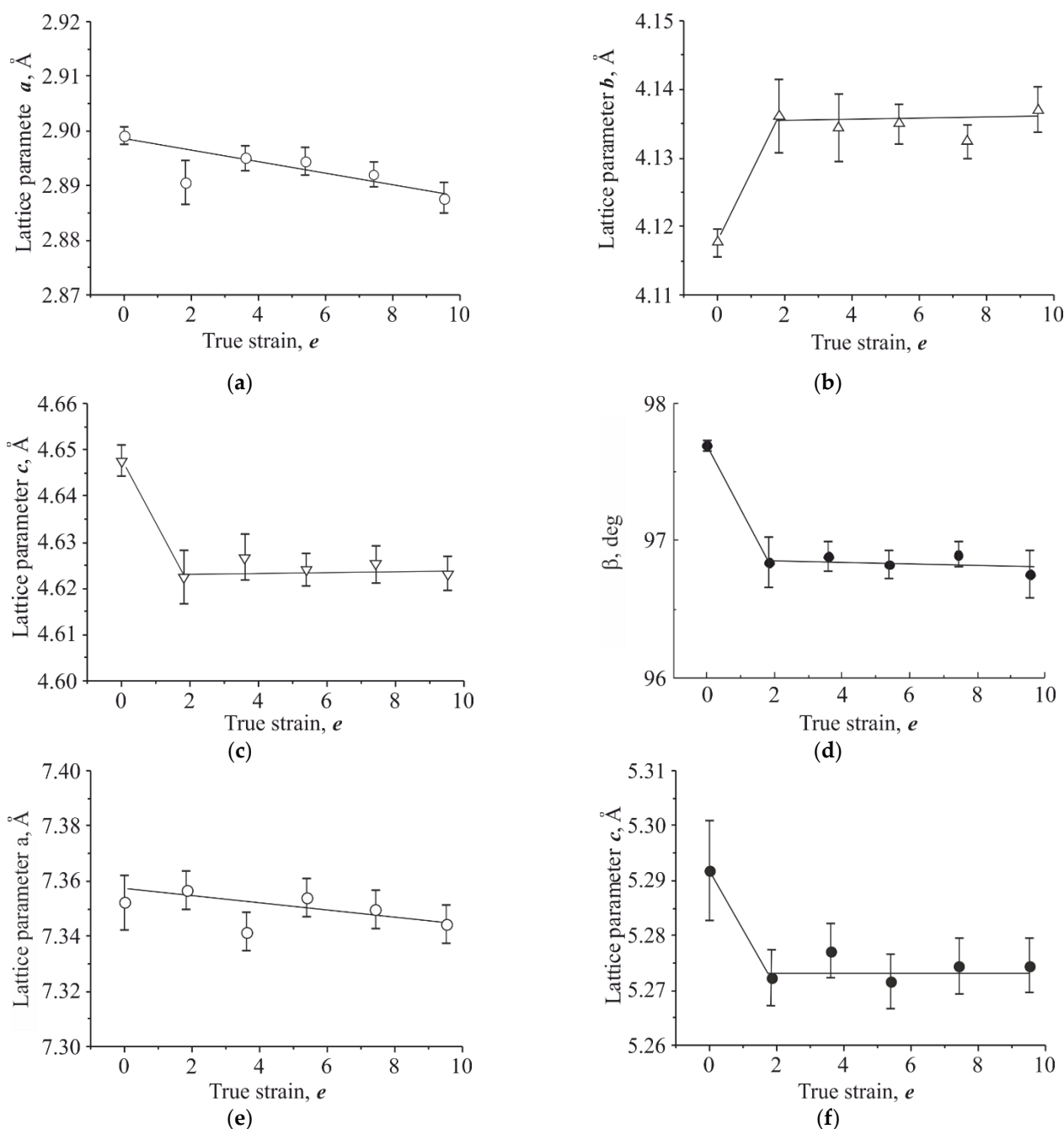

Figure 2. Fragments of XRD spectra of Ti$_{49.8}$Ni$_{50.2}$ at room temperature (Co-Kα radiation) after *abc* pressing to different true strains: ▼—B19′, ◆—R, and ●—B2.

At room temperature, the initial alloy revealed B19′ reflections and traces of R reflections, while any B2 reflections were absent. Another situation was observed after *abc* pressing to *e* = 1.84. First, at room temperature, the main volume of all specimens contained

R and B19′ phases. Second, the positions of B19′ peaks were markedly shifted compared to those in the initial alloy. As the strain *e* increased, their angular position changed little.
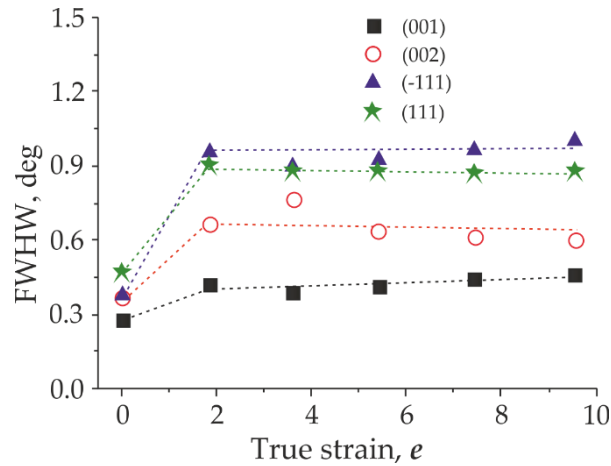
Figure 3 shows the R and B19′ lattice parameters at different true strains. It can be seen that at *e* = 1.84, the B19′ lattice parameter *a* decreased somewhat, and further, it weakly depended on *e* (Figure 3a). At the same time, the parameters *b*, *c*, and the angle β at *e* = 1.84 changed steeply, and further, their *e* dependence weakened (Figure 3b–d). The R lattice parameters *a* and *b* after *abc* pressing remained almost the same as before *abc* pressing (Figure 3e), whereas the parameter *c* decreased markedly at *e* = 1.84, and further, it weakly depended on *e* (Figure 3f).

Figure 3. Effect of true *abc* strain in Ti$_{49.8}$Ni$_{50.2}$ on lattice parameters *a* (**a**), *b* (**b**), *c* (**c**), and monoclinic angle β (**d**) of the B19′ phase and the lattice parameters *a* (**e**) and *b* (**f**) of the R phase.
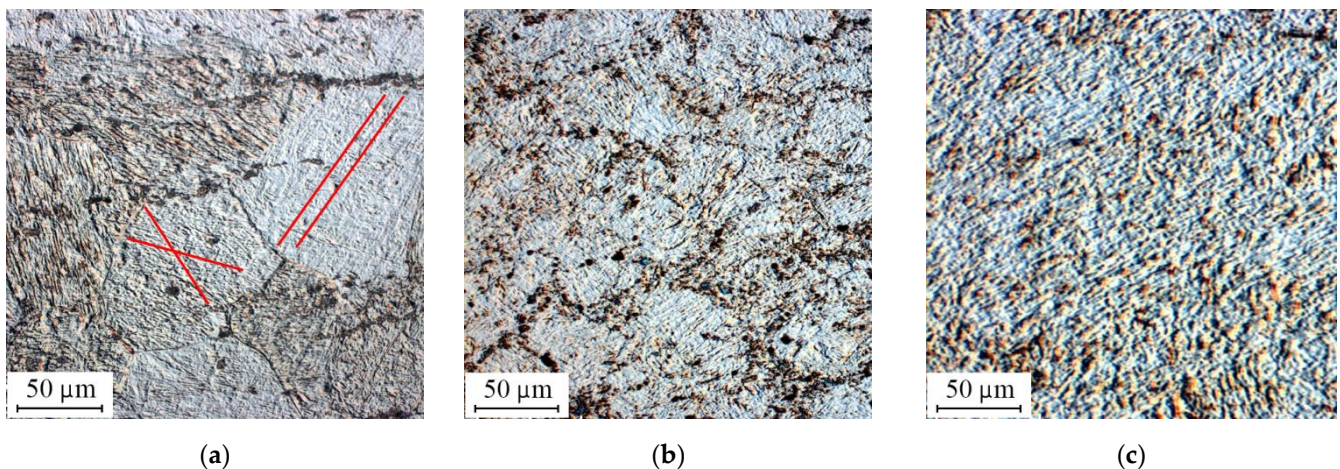
Figure 4 shows the full-width at half maximum (FWHM) of the most intense B19′ peaks at different true strains. It can be seen that at e = 1.84, the FWHM of these peaks increased steeply, and further, their weak dependence on e can be observed.

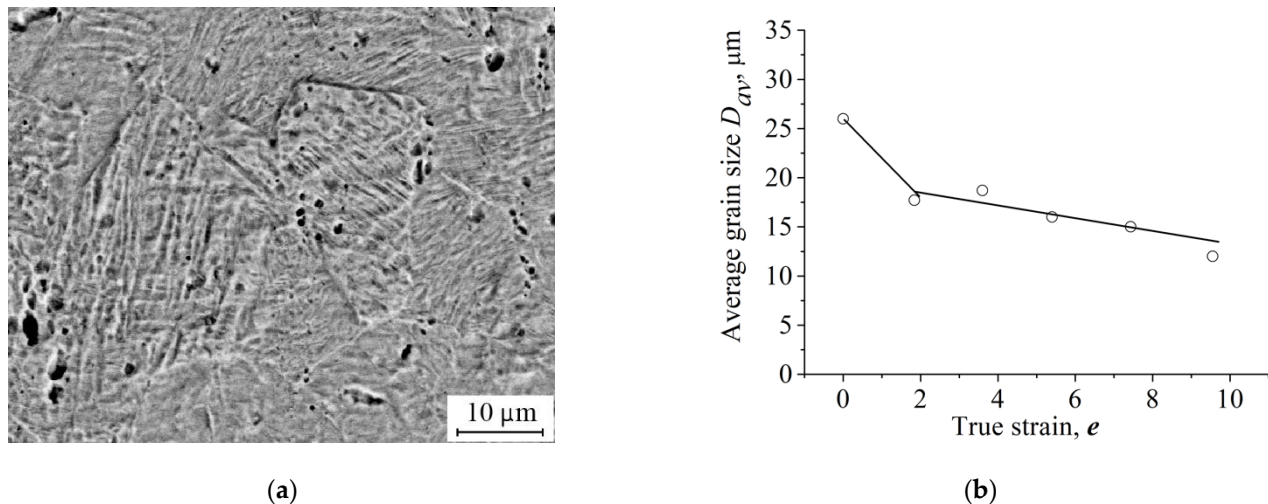**Figure 4.** The full-width at half maximum (FWHM) of the most intense B19′ peaks versus true *abc* strain in Ti$_{49.8}$Ni$_{50.2}$.

3.3. Microstructure

The microstructure of Ti$_{49.8}$Ni$_{50.2}$ before and after *abc* pressing with different true strains can be evaluated from its images in Figure 5. Such images taken by differential interference contrast (DIC) microscopy were used to estimate the average grain size. First, the number of grains within an image was determined and the average grain area was calculated; then, the grain shape was approximated by squares with a side that was taken equal to the average grain size. The initial alloy revealed rather clear-cut grain boundaries (Figure 5a) such that the number of grains was well identifiable. In some grains, the deformation relief was represented by rather thin similarly directed bands, and in the others, by two systems of intersecting bands (red lines). In their adjacent grains, the band direction was different. It is not improbable that martensite plates are in the images. As the *abc* strain increased, the identification of grain boundaries by DIC microscopy became difficult (Figure 5b), and at e = 9.55, they were almost invisible (Figure 5c). Therefore, highly magnified SEM images were used for their identification at such strains.

Figure 5. DIC images of Ti$_{49.8}$Ni$_{50.2}$ before (**a**) and after *abc* pressing to e = 3.6 (**b**) and e = 9.55 (**c**).

The grain size in $Ti_{49.8}Ni_{50.2}$ at $e = 5.4$ can be evaluated from its SEM image in Figure 6a and the dependence of the average grain size on the true strain from Figure 6b. The dependence suggests that the most noticeable change in the average grain size falls on $e = 1.84$. As e increased, the average grain size decreased linearly with e, and this decrease was slight compared to that at $e = 1.84$. Such changes occurred in the coarse grain structure of the alloy at $e = 9.55$, and the average grain size was $D_{av} \approx 12$ µm.

(**a**)   (**b**)

Figure 6. SEM image of $Ti_{49.8}Ni_{50.2}$ with a true *abc* strain $e = 5.4$ (**a**) and e dependence of the average grain size D_{av} (**b**).
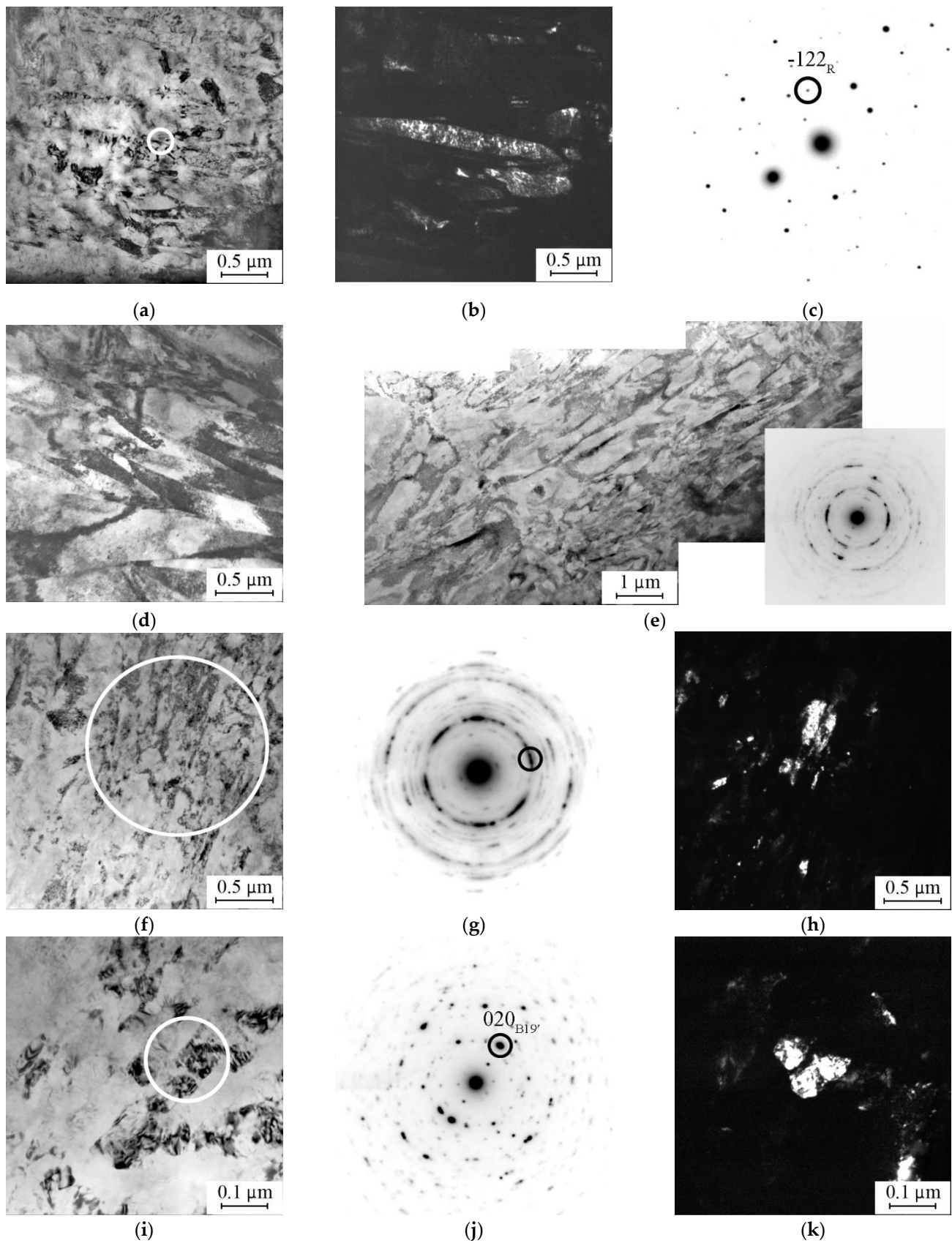
The influence of *abc* pressing on the microstructure and phase state of the alloy was analyzed by transmission electron microscopy and selected area diffraction, which confirmed the results of our XRD analysis. At room temperature, the initial and *abc* pressed specimens, irrespective of the true strain, contained R and B19′ phases. Their reflections in the initial alloy and alloy *abc* pressed at $e = 9.55$ are marked in Figure 7c and Figure 7g,j, respectively. In all specimens, no B2 phase was found.

As can be seen from bright-field TEM images (Figure 7a,d–f,i), the microstructure of all specimens, whether initial or *abc* pressed, featured differently directed bands of length 1–4 µm and width 0.5 µm, which were particularly evident at rather low magnification (Figure 7e). Such bands were also distinguished on many dark-field TEM images (Figure 7b). From comparison of the characteristic band sizes on DIC and SEM images (Figures 5 and 6a) it follows that such a band microstructure is the internal structure of bands of the deformation relief. In this sense, the bands of the deformation relief can be considered as mesoscale structural elements.
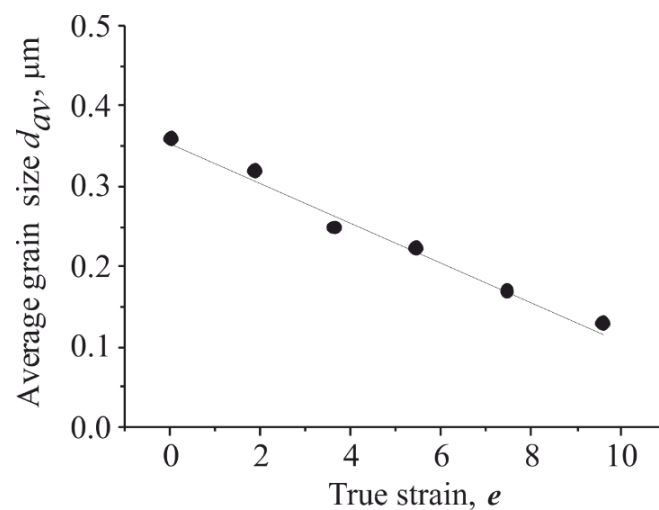
Our analysis shows that the initial specimens are normally characterized by R and B19′ point reflections on their microdiffraction patterns. Such a pattern from the R region, circled in Figure 7a, is shown in Figure 7c. As the true strain increased, the microdiffraction pattern from the region selected with a diaphragm with a diameter ≈ 1 µm (circled in Figure 7a) gradually took the form of a ring (Figure 7e,g), which is indicative of microscale grain–subgrain refinement. With a diaphragm with a diameter of 115 nm, the corresponding region (circled in Figure 7i) showed only point reflections (Figure 7j), suggesting that the size of the microscale grains–subgrains formed at $e = 9.55$ was at least 100 nm.

The average grain–subgrain size, d_{av}, was determined from dark-field images such as those shown in Figure 7b,h,k. First, the absolute area of each luminous region was determined and then all such regions were approximated by a square with a side length that was taken equal to d_{av}. The results are presented in Figure 8. As can be seen from the figure, the average grain–subgrain size d_{av}, according to TEM, decreased almost linearly with the increase in the true strain, and at $e = 9.55$, it measured approximately 130 nm.

Figure 7. TEM images and diffraction patterns of $Ti_{49.8}Ni_{50.2}$ before (**a**–**c**) and after *abc* pressing to e = 1.84 (**d**), e = 5.4 (**e**), and e = 9.55 (**f**–**k**).

Figure 8. Average grain–subgrain size d_{av} versus true *abc* strain in Ti$_{49.8}$Ni$_{50.2}$ according to TEM.

4. Discussion
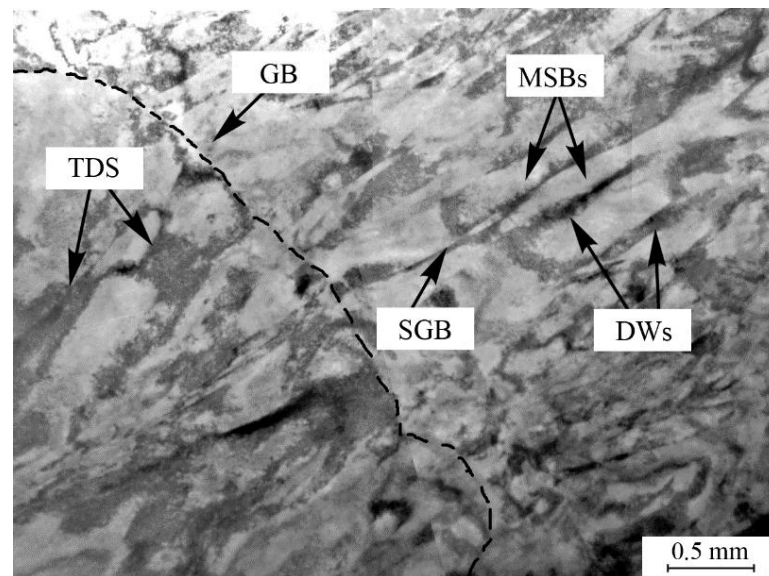
Our study shows that after *abc* pressing at 573 K, the temperatures of direct and reverse martensite transformations in Ti$_{49.8}$Ni$_{50.2}$ was 15–20 K lower than those after *abc* pressing at 723 K [19]. In other words, the microstructure of the alloy *abc* pressed at 573 K stabilized its B2 phase and impeded the transition to martensite on cooling. After *abc* pressing at 573 K, no sign of aging and Ti$_3$Ni$_4$ precipitation were found in the alloy to explain the observed decrease in the temperatures of martensite transformations. Thus, this decrease can be provided only by crystalline defects and associated internal stresses induced by *abc* pressing. Likely, the number of defects and the value of internal stresses after *abc* pressing at 573 K was higher than those after *abc* pressing at 723 K due to the less intense recovery processes [19–21,29].

The steep decrease in the temperatures M$_S$ and M$_f$ after *abc* pressing to *e* = 1.84 suggests that even this true strain provided the formation of a microstructure with a high defect density in the alloy. Their weaker dependence on the true strain at *e* > 1.84 indicates that although such a strain does increase the crystalline defect density in the volume of grains–subgrains, this increase is insignificant compared to its level at *e* = 1.84.
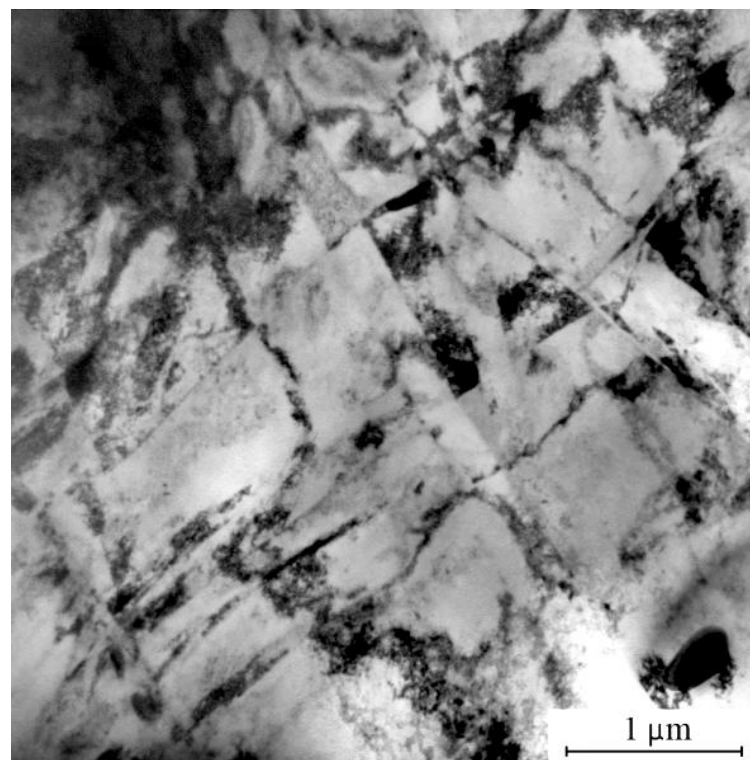
The formation of crystalline defects during *abc* pressing was confirmed by our XRD data (Figures 2–4), which revealed an increase in the peak halfwidth as evidence that the density of the crystalline defects increased and the size of coherent scattering regions decreased. Even after *abc* pressing to *e* = 1.84, the material showed a steep increase in the amount of its R phase induced by internal stresses. Moreover, it was the effect of internal stresses from crystalline defects and associated lattice distortion that are responsible for the observed substantial change in the angular position of B19′ peaks and in the lattice parameters.

According to our TEM data, the microstructure of Ti$_{49.8}$Ni$_{50.2}$ after *abc* pressing is, in many ways, similar to that of fcc alloys after severe plastic deformation. Figure 9 shows an enlarged fragment of the TEM image in Figure 7e with arrows pointing to five characteristic elements of the alloy microstructure after *abc* pressing to *e* = 5.4: a grain boundary (GB), a subgrain boundary (SGB), dislocation walls (DWs), tangled dislocation structure (TDS), and microshear bands (MSBs). Such a representation can also be found elsewhere [42]. The data suggest that the mechanisms of grain–subgrain refinement in Ti$_{49.8}$Ni$_{50.2}$ are essentially no different from those in other materials deformed by SPD methods [1,4,8]. Reasoning from our study, we think that two parallel mechanisms of grain–subgrain refinement operate in Ti$_{49.8}$Ni$_{50.2}$ during *abc* pressing. One of the mechanisms is the formation of a cellular dislocation substructure that transforms into a grain–subgrain structure due to the generation of dislocations and to their escape into the cell walls. The other mechanism of grain–subgrain refinement is the formation of intersecting microshear bands in the volume

of grains (Figure 10). Although the dislocation substructure in our study was not addressed at length, some features of its behavior during *abc* pressing were evident in our experiments. In particular, after the first cycle of *abc* pressing, the scalar density of dislocations increased greatly, and after the next ones, its increase was small. Now, experiments with an XRD analysis of dislocation densities are being conducted. Their results will soon be published.

Figure 9. Characteristic microstructural elements of Ti$_{49.8}$Ni$_{50.2}$ after *abc* pressing to *e* = 5.4: GB—grain boundary, SGB—subgrain boundary, DWs—dislocation walls, TDS—tangled dislocation structure, MSBs—microshear bands; (enlarged fragment of TEM image in Figure 7e).

Figure 10. Intersecting microshear bands in grain volume after *abc* pressing to *e* = 1.84.

There is no doubt that the microstructural elements formed in the alloy during *abc* pressing influenced its mechanical and functional properties to one or another extent. However, the available research data are insufficient for any unambiguous conclusions on the efficiency of these elements, which necessitates further experimental studies on the mechanical and functional properties of the alloy and precision analyses of its microstructure.

The effect of severe plastic deformation on the properties of metals and alloys is associated with grain–subgrain refinement. The criterion is the size of grains–subgrains. In most studies, the initial materials are annealed (recrystallized) ones with clearly visible high-angle grain boundaries on their metallographic sections. The average grain size at small true strains is determined by light microscopy, and the size of grains–subgrains at high true strains is determined from dark-field TEM images almost without regard for differences between grains with high-angle boundaries and subgrains with low-angle boundaries. However, as demonstrated by our experimental data in Section 3.3, even small true strains can provide the formation of micron and submicron elements (microshear bands, subgrains, and possibly grains), and on dark-field TEM images, such elements can be broken into fine fragments. As a result, any quantitative estimates of the average grain–subgrain size are uncertain. In our opinion, the refinement of grain–subgrain structures under severe plastic deformation can conveniently be described in the context of structural scales. On the macroscale, we have a decrease in the average size of parent grains which can be measured by light microscopy, and on the microscale, the volume of parent grains acquires a grain–subgrain structure that can be measured by transmission electron microscopy. On the microscale, the deformation of metals and alloys results in crystalline defects (vacancies, interstitial atoms, dislocations, microshear bands), and their motion and interaction can lead to the formation of various hierarchical structures [43].

In our study, the most significant decrease in the grain size on the macroscale was provided by the first cycle of *abc* pressing (Figure 6), and the refinement of parent grains in the next cycles was less intense. At the same time, the average grain–subgrain size at the microscale decreased linearly with the increase in the true strain (Figure 8).

Thus, our experimental results show that even the first cycle of *abc* pressing at 573 K produced substantial changes in the microstructure of $Ti_{49.8}Ni_{50.2}$. The results can be used in models descriptive of the mechanisms by which the microstructure of TiNi alloys influences their mechanical and functional properties.

5. Conclusions

The results of our study and their comparison with other related data allow for the following conclusions on the microstructure of $Ti_{49.8}Ni_{50.2}$ *abc* pressed at T = 573 K.

1. As the true strain *e* increased, the grain–subgrain structure of $Ti_{49.8}Ni_{50.2}$ was refined on different scales at a time: through decreasing the average size of parent grains on the macroscale and the size of grains–subgrains in the volume of parent grains on the microscale;
2. The average grain–subgrain size attained after *abc* pressing to *e* = 9.55 at 573 K was approximately 130 nm;
3. The alloy *abc* pressed at 573 K revealed a decrease in all martensite transformation temperatures, a change in the lattice parameters, R phase formation, and angular shifts of diffraction peaks and their broadening because the number of structural defects became larger;
4. The largest change in the microstructure of $Ti_{49.8}Ni_{50.2}$ on all scales was provided by *abc* pressing to *e* = 1.84. Increasing the true strain to *e* = 9.55 gave a much smaller effect, suggesting that the alloy obtained a high density of structural defects even at *e* = 1.84;
5. Likely, the grain–subgrain structure of $Ti_{49.8}Ni_{50.2}$ during *abc* pressing was refined by two parallel mechanisms: through the formation of a cellular dislocation substructure with its further transformation into a grain–subgrain structure and through the formation of intersecting microshear bands in the volume of grains.

References

1. Estrin, Y.; Vinogradov, A. Extreme grain refinement by severe plastic deformation: A wealth of challenging science. *Acta Mater.* **2013**, *61*, 782–817. [CrossRef]
2. Meyers, M.A.; Mishra, A.; Benson, D.J. Mechanical properties of nanocrystalline materials. *Prog. Mater. Sci.* **2006**, *51*, 427–556. [CrossRef]
3. Valiyev, R.Z.; Aleksandrov, I.A. *Bulk Nanostructure Metal Materials: Obtaining, Structure and Properties*; Akademkniga: Moscow, Russian, 2007; p. 398.
4. Pippan, R.; Scheriau, S.; Taylor, A.; Hafok, M.; Hohenwarter, A.; Bachmaier, A. Saturation of Fragmentation during Severe Plastic Deformation. *Annu. Rev. Mater. Res.* **2010**, *40*, 319–343. [CrossRef]
5. Sakai, T.; Belyakov, A.; Kaibyshev, R.; Miura, H.; Jonas, J.J. Dynamic and post-dynamic recrystallization under hot, cold and severe plastic deformation conditions. *Prog. Mater. Sci.* **2014**, *60*, 130–207. [CrossRef]
6. Valiev, R.; Estrin, Y.; Horita, Z.; Langdon, T.; Zehetbauer, M.; Zhu, Y. Fundamentals of superior properties in bulk nanoSPD materials. *Mater. Res. Lett.* **2016**, *4*, 1–21. [CrossRef]
7. Valiev, R.Z.; Estrin, Y.; Horita, Z.; Langdon, T.G.; Zehetbauer, M.J.; Zhu, Y. Producing bulk ultrafine-grained materials by severe plastic deformation: Ten years later. *JOM* **2016**, *68*, 1216–1226. [CrossRef]
8. Bagherpour, E.; Pardis, N.; Reihanian, M.; Ebrahimi, R. An overview on severe plastic deformation: Research status, techniques classification, microstructure evolution, and applications. *Int. J. Adv. Manuf. Technol.* **2019**, *100*, 1647–1694. [CrossRef]
9. Lopatin, Y.G.; Chuvildeev, V.N.; Nokhrin, A.V.; Kopylov, V.I.; Pirozhnikova, O.E.; Sakharov, N.V.; Piskunov, A.V.; Melyokhin, N.V. The effect of temperature in severe plastic deformation on grain refinement limit in metals and alloys. *Vestn. Lobachevsky State Univ. Nizhni Novgorod* **2010**, *5*, 132–137.
10. Prokofyev, E.A. Structure and properties of ultra-low grain TiNi alloy obtained by intensive plastic deformation. *Vestn. UGATU* **2006**, *8*, 169–174.
11. Yurchenko, L.I.; Dyupin, A.P.; Gunderov, D.V.; Valiev, R.Z.; Kuranova, N.N.; Pushin, V.G.; Uksusnikov, A.N. Mechanical Properties and Structure of High-Strength Nanostructured Nickel-Titanium Alloys Subjected to ECAP and Rolling. *Faz. Perekh. Uporyad. Sost. Novye Mater.* **2006**. Available online: http://www.ptosnm.ru (accessed on 4 October 2006).
12. Khmelevskaya, I.Y.; Prokoshkin, S.D.; Trubitsyna, I.B.; Belousov, M.N.; Dobatkin, S.V.; Tatyanin, E.V.; Korotitskiy, A.V.; Brailovski, V.; Stolyarov, V.V.; Prokofiev, E.A. Structure and properties of Ti–Ni-based alloys after equal-channel angular pressing and high-pressure torsion. *Mater. Sci. Eng. A* **2008**, *481–482*, 119–122. [CrossRef]
13. Kreitcberg, A.; Brailovski, V.; Prokoshkin, S.; Gunderov, D.; Khomutov, M.; Inaekyan, K. Effect of the grain/subgrain size on the strain-rate sensitivity and deformability of Ti–50 at%Ni alloy. *Mater. Sci. Eng. A* **2015**, *622*, 21–29. [CrossRef]
14. Shahmir, H.; Nili-Ahmadabadi, M.; Mansouri-Arani, M.; Langdon, T.G. The processing of NiTi shape memory alloys by equal-channel angular pressing at room temperature. *Mater. Sci. Eng. A* **2013**, *576*, 178–184. [CrossRef]
15. Lotkov, A.I.; Grishkov, V.N.; Kashin, O.A.; Baturin, A.A.; Zhapova, D.Y.; Timkin, V.N. Mechanisms of microstructure evolution in TiNi-based alloys under warm deformation and its effect on martensite transformations. In *Shape Memory Alloys: Properties, Technologies, Opportunities*; Resnina, N., Rubanic, V., Eds.; Materials Science Foundations; Trans. Tech. Publ. Ltd.: Pfäffikon, Switzerland, 2015; Volume 81–82, pp. 245–259. [CrossRef]
16. Lotkov, A.I.; Grishkov, V.N.; Dudarev, E.F.; Koval, Y.N.; Girsova, N.V.; Kashin, O.A.; Tabachenko, A.N.; Firstov, G.S.; Timkin, V.N.; Zhapova, D.Y. Ultrafine Structure and Martensitic Transformation in Titanium Nickelide after Warm abc Pressing. *Inorg. Mater. Appl. Res.* **2011**, *2*, 548–555. [CrossRef]
17. Lotkov, A.I.; Grishkov, V.N.; Baturin, A.A.; Dudarev, E.F.; Zhapova, D.Y.; Timkin, V.N. The effect of warm deformation by abc-pressing method on mechanical properties of titanium nickelide. *Lett. Mater.* **2015**, *5*, 170–174. [CrossRef]
18. Lotkov, A.I.; Grishkov, V.N.; Dudarev, Y.F.; Girsova, N.V.; Tabachenko, A.N. Formation of ultrafine grain structure, martensitic transformations and unelastic properties of titanium nickelide after abc-pressing. *Vopr. Materialoved.* **2008**, *1*, 161–165.
19. Lotkov, A.; Grishkov, V.; Zhapova, D.; Timkin, V.; Baturin, A.; Kashin, O. Superelasticity and shape memory effect after warm abc-pressing of TiNi-based alloy. *Mater. Today Proc.* **2017**, *4*, 4814–4818. [CrossRef]

20. Lotkov, A.I.; Kashin, O.A.; Grishkov, V.N.; Krukovskii, K.V. The influence of degree of deformation under isothermal abc pressing on evolution of structure and temperature of phase transformations of alloy based on titanium nickelide. *Inorg. Mater. Appl. Res.* **2015**, *6*, 96–104. [CrossRef]

21. Zhapova, D.Y.; Lotkov, A.I.; Grishkov, V.N.; Timkin, V.N.; Rodionov, I.S.; Kolevatov, A.S.; Belosludtseva, A.A. Inelastic properties of titanium nickelide after warm abc-pressing. *Izv. Vyssh. Uchebn. Zaved. Fiz.* **2016**, *59*, 60–63.

22. Kashin, O.; Krukovskii, K.; Lotkov, A.; Grishkov, V. Effect of True Strains in Isothermal abc Pressing on Mechanical Properties of Ti$_{49.8}$Ni$_{50.2}$ Alloy. *Metals* **2020**, *10*, 1313. [CrossRef]

23. Gunderov, D.; Lukyanov, A.; Prokofiev, E.; Kilmametov, A.; Pushin, V.; Valiev, R. Mechanical properties and martensitic transformations in nanocrystalline Ti$_{49.4}$Ni$_{50.6}$ alloy produced by high-pressure torsion. *Mater. Sci. Eng. A* **2009**, *503*, 75–77. [CrossRef]

24. Gunderov, D.; Lukyanov, A.; Prokofiev, E.; Pushin, V.G. Mechanical properties of the nanocrystalline Ti$_{49.4}$Ni$_{50.6}$ alloy produced by High Pressure Torsion. *Eur. Phys. J. Spec. Top.* **2008**, *158*, 53–58. [CrossRef]

25. Kockar, B.; Karaman, I.; Kulkarni, A.; Chumlyakov, Y.; Kireeva, I.V. Effect of severe ausforming via equal channel angular extrusion on the shape memory response of a NiTi alloy. *J. Nucl. Mater.* **2007**, *361*, 298–305. [CrossRef]

26. Potapova, A.A.; Stolyarov, V.V. Deformability and structural features of shape memory TiNi alloys processed by rolling with current. *Mater. Sci. Eng. A* **2013**, *579*, 114–117. [CrossRef]

27. Shahmir, H.; Nili-Ahmadabadi, M.; Huang, Y.; Jung, J.M.; Kim, H.S.; Langdon, T.G. Shape memory characteristics of a nanocrystalline TiNi alloy processed by HPT followed by post-deformation annealing. *Mater. Sci. Eng. A* **2018**, *734*, 445–452. [CrossRef]

28. Shahmir, H.; Nili-Ahmadabadi, M.; Huang, Y.; Jung, J.M.; Kim, H.S.; Langdon, T.G. Shape memory effect in nanocrystalline NiTi alloy processed by high-pressure torsion. *Mater. Sci. Eng. A* **2015**, *626*, 203–206. [CrossRef]

29. Shamsolhodaei, A.; Zarei-Hanzaki, A.; Moghaddam, M. Structural and functional properties of a semi equiatomic NiTi shape memory alloy processed by multi-axial forging. *Mater. Sci. Eng. A* **2017**, *700*, 1–9. [CrossRef]

30. Shri, D.N.A.; Tsuchiya, K.; Yamamoto, A. Surface characterization of TiNi deformed by high-pressure torsion. *Appl. Surf. Sci.* **2014**, *289*, 338–344. [CrossRef]

31. Tong, Y.X.; Chen, F.; Guo, B.; Tian, B.; Li, L.; Zheng, Y.F.; Gunderov, D.V.; Valiev, R.Z. Superelasticity and its stability of an ultrafine-grained Ti$_{49.2}$Ni$_{50.8}$ shape memory alloy processed by equal channel angular pressing. *Mater. Sci. Eng. A* **2013**, *587*, 61–64. [CrossRef]

32. Tong, Y.X.; Hu, K.P.; Chen, F.; Tian, B.; Li, L.; Zheng, Y.F. Multiple-stage transformation behavior of Ti49.2Ni50.8 alloy with different initial microstructure processed by equal channel angular pressing. *Intermetallics* **2017**, *85*, 163–169. [CrossRef]

33. Valiev, R.; Gunderov, D.; Prokofiev, E.; Pushin, V.; Zhu, Y. Nanostructuring of TiNi alloy by SPD processing for advanced properties. *Mater. Trans.* **2008**, *49*, 97–101. [CrossRef]

34. Zhang, X.; Song, J.; Huang, C.; Xia, B.; Chen, B.; Sun, X.; Xie, C. Microstructures evolution and phase transformation behaviors of Ni-rich TiNi shape memory alloys after equal channel angular extrusion. *J. Alloys Compd.* **2011**, *509*, 3006–3012. [CrossRef]

35. Gunderov, D.V.; Pushin, V.G.; Valiev, R.Z.; Prokofiev, E.A. Investigation of the nature of the high strength and ductility of the ultrafine-grained TiNi alloy obtained by equal-channel angular compression. *Deform. Fract. Mater.* **2007**, *10*, 13–21.

36. Kuranova, N.N.; Gunderov, D.V.; Ukusnikov, A.N.; Luk'yanov, A.V.; Yurchenko, L.I.; Prokof'ev, E.A.; Pushin, V.G.; Valiev, R.Z. Effect of heat treatment on the structural and phase transformations and mechanical properties of TiNi alloys subjected to severe plastic deformation. *Phys. Met. Metallogr.* **2009**, *108*, 556–568. [CrossRef]

37. Prokoshkin, S.D.; Khmelevskaya, I.Y.; Dobatkin, S.V.; Trubitsyna, I.B.; Tat'yanin, E.V.; Stolyarov, V.V.; Prokof'ev, E.A. Structure evolution under severe plastic deformation of shape memory alloys based on titanium nickelide. *Phys. Met. Metallogr.* **2004**, *97*, 619–625.

38. Stolyarov, V.V.; Prokofiev, E.A.; Prokoshkin, S.D.; Dobatkin, S.V.; Trubitsyna, I.B.; Khmelevskaya, I.Y.; Pushin, V.G.; Valiev, R.Z. Structure, mechanical properties, and shape memory effect in TiNi alloys exposed to equal channel angular pressing. *Phys. Met. Metallogr.* **2005**, *100*, 91–102.

39. Churakova, A.A.; Gunderov, D.V.; Lukyanov, A.V.; Lebedev, Y.A. Effect of thermal cycling in the range of phase transformation B2–B19′ on the microstructure and mechanical properties of UFG alloy Ti$_{49.8}$Ni$_{50.2}$. *Lett. Mater.* **2013**, *3*, 166–168. [CrossRef]

40. Kudoh, Y.; Tokonami, M.; Miyazaki, S.; Otsuka, K. Cristal structure of the martensite in Ti+49.2 at. % Ni alloy analyzed by the single crystal X-ray diffraction method. *Acta Metall.* **1985**, *33*, 2049–2056. [CrossRef]

41. Sitepu, H. Use of synchrotron diffraction data for describing crystal structures and crystallographic phase analysis of R-phase NiTi shape memory alloy. *Textures Micrjstruct.* **2003**, *35*, 185–195. [CrossRef]

42. Huang, J.Y.; Zhu, Y.T.; Jiang, H.; Lowe, T.C. Microstructures and dislocation configurations in nanostructured Cu processed by repetitive corrugation and straightening. *Acta Mater.* **2001**, *49*, 1497–1505. [CrossRef]

43. Panin, V.E.; Likhachev, V.A.; Grinyaev, Y.V. *Structural Levels of Deformation in Solids*; Nauka: Novosibirsk, Russia, 1985; p. 255. (In Russian)